Mesoporous Silica Nanoparticles for Active Corrosion Protection

Dimitriya Borisova,* Helmuth Möhwald, and Dmitry G. Shchukin

Max Planck Institute of Colloids and Interfaces, Am Mühlenberg 1, 14424 Potsdam-Golm, Germany

ABSTRACT This work presents the synthesis of monodisperse, mesoporous silica nanoparticles and their application as nanocontainers loaded with corrosion inhibitor (1*H*-benzotriazole (BTA)) and embedded in hybrid SiO_x/ZrO_x sol−gel coating for the corrosion protection of aluminum alloy. The developed porous system of mechanically stable silica nanoparticles exhibits high surface area ($\sim$1000 $m^2 \cdot g^{-1}$), narrow pore size distribution ($d \sim 3$ nm), and large pore volume ($\sim$1 $mL \cdot g^{-1}$). As a result, a sufficiently high uptake and storage of the corrosion inhibitor in the mesoporous nanocontainers was achieved. The successful embedding and homogeneous distribution of the BTA-loaded monodisperse silica nanocontainers in the passive anticorrosive SiO_x/ZrO_x film improve the wet corrosion resistance of the aluminum alloy AA2024 in 0.1 M sodium chloride solution. The enhanced corrosion protection of this newly developed active system in comparison to the passive sol−gel coating was observed during a simulated corrosion process by the scanning vibrating electrode technique (SVET). These results, as well as the controlled pH-dependent release of BTA from the mesoporous silica nanocontainers without additional polyelectrolyte shell, suggest an inhibitor release triggered by the corrosion process leading to a self-healing effect.

KEYWORDS: silica · nanoparticles · inhibitor · release · sol−gel coating · active corrosion protection

Corrosion has been an extremely important issue mankind has been trying to understand and control since starting to use metal objects. The process of corrosive degradation of materials is not only of great complexity but also of enormous economic importance. As a very important example, the aluminum alloy AA2024, which is extensively used in the aircraft industry because of its optimum weight and strength, exhibits resistance to general corrosion due to the formation of a natural, inert, and protective oxide layer. However, due to its intermetallic inclusions, it is susceptible to localized pitting corrosion, which leads to exfoliation corrosion with destructive consequences for the structural integrity of the alloy.[1] Currently, its corrosion protection is accomplished by deposition of pretreatment, primer, and top-coat layers. The most effective corrosion inhibition relies extensively on hexavalent chromium compounds included in the protective coating.[2] However, the use of chromates and other chromium-containing compounds has been restricted worldwide due to their toxic and carcinogenic character.[3] This has resulted in high scientific interest and research activity in finding environmentally friendly Cr^{6+} replacements, exhibiting high performance corrosion protection.

The sol−gel method is quite promising for preparation of inorganic protective coatings with high corrosion inhibition efficiency.[4] Silane and siloxane-based films exhibit not only good adhesion to both metallic substrates and organic top coats but also good barrier properties due to a dense −Si−O−Si− network.[5] Unfortunately, in the presence of microcracks or small defects in the coating, the penetration of aggressive species toward the metallic surface cannot be prevented. The tendency of the protective film to build pores and cracks can be decreased by incorporating nanoparticles (NPs), which contribute to the passive obstruction of corrosion initiation.[6−8] In addition, the mechanical stability and thickness of the silane layer can be enhanced by this approach. However, these systems act only as passive physical barriers and, in comparison to the chromium approach, cannot hinder corrosion propagation actively in the case of a local failure of the coating. Addition of inorganic or organic inhibitors to the sol−gel coating was reported to be a feasible way to decrease the corrosion rate when the protective barrier layer gets damaged and thus to attain active, self-healing properties.[9−11] Nevertheless, a too high concentration or unsatisfactory solubility of the inhibiting agents can deteriorate the integrity and physical barrier properties of the coating matrix.[12]

A promising approach to overcome the drawbacks of the above-mentioned strategies for improving the anticorrosive sol−gel barrier coatings is to combine them. Therefore, the embedded nanoparticles should additionally serve as nanocontainers encapsulating

* Address correspondence to borisova@mpikg.mpg.de.

Received for review November 2, 2010 and accepted February 15, 2011.

Published online February 23, 2011
10.1021/nn102871v

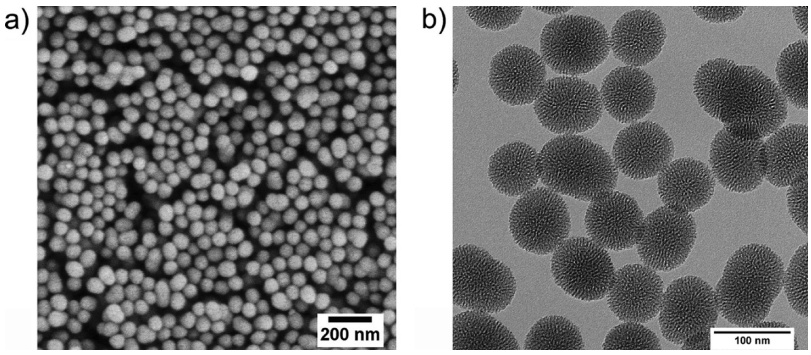

Figure 1. (a) SEM and (b) TEM micrographs of mesoporous silica nanoparticles.

the active inhibiting agent, preventing its direct interaction with the sol−gel matrix and controlling its release. In order to obtain the aimed high corrosion inhibition efficiency, the embedded nanocontainers should also possess good compatibility with the sol−gel matrix components, monodisperse sizes in the range below 200 nm, and have a homogeneous distribution in the coating to keep its integrity and barrier properties. Attempts to fulfill the above stated requirements have been made by employing metal oxide NPs coated with polyelectrolyte multilayers and loaded with organic corrosion inhibitor.[13−15] It was shown that a layer-by-layer assembled shell can provide controlled inhibitor release in response to local pH changes and thereby enhanced corrosion protection. Despite the clear advantages of the studied systems, their complexity restricts their up-scaling and industrial application. Recently, more simple halloysite containers without a polyelectrolyte shell were demonstrated to be suitable nanocontainers for storage and gradual release of anticorrosive agents.[16] However, the biggest drawbacks of all these approaches is the low concentration of loaded inhibitor (less than 17 wt %) and long release time, which as a result limits the anticorrosive performance.

This work describes a new contribution to the design of anticorrosive sol−gel coatings by the application of monodisperse mesoporous silica NPs as containers for anticorrosive organic inhibiting agent. Owing to their high pore volume and surface area, a loading inhibitor capacity that is at least two times greater than previously reported ones has been achieved. The NPs also possess high mechanical stability which preserves the pore and particle integrity. These properties allow for both the corrosion inhibitor storage in the porous protective matrix and its release in response to pH changes induced by the corrosion process. Furthermore, the good compatibility of the nanocontainers with the components of the SiO_x/ZrO_x sol−gel film allows for easy incorporation into the coating matrix. As a result, an enhanced corrosion protection for aluminum alloy AA2024 by means of a simplified system consisting of a hybrid silica−zirconia film doped with 1*H*-benzotriazole-loaded silica nanocarriers is demonstrated.

Hence, we describe here a very general and technically feasible approach to achieve an active corrosion protection coating that may find broad use beyond the actual metal to be protected and also beyond the specific agent and coating to be used.

RESULTS AND DISCUSSION

Mesoporous Silica Nanoparticles (MS-SiO_2-NPs). The mesoporous silica NPs synthesized applying the procedure introduced by Möller *et al.*[17] are in the form of a white stable colloidal water suspension. The small polydispersity index (0.07) derived from dynamic light scattering (DLS) measurements indicates good colloidal stability and narrow particle size distribution. The measured *Z*-average diameter (129 nm) and the calculated average particle diameter excluding the hydrosolvation shell (104 nm) are bigger than the actual diameters found in the electron micrographs (70−90 nm). This suggests the presence of intergrown particles and agglomerates. However, the SEM and TEM investigations (Figure 1a,b) indicate that their fraction is negligible and confirm the relative monodispersity of the samples. All particles exhibit spherical shape and smooth surface. The zeta-potential measurement results (−12.4 mV at pH 6) of silica in water suspensions are in agreement with literature.[18] Such negative values are expected at pH values above the isoelectric point (pH 5) found for the synthesized silica NPs (Figure 2).

The TEM images reveal a well-developed pore structure. In all particles, the pores are open, not ordered and oriented from the center to the outer surface, building a complex, worm-like pore system. The adsorption−desorption behavior of N_2 in the silica NPs delivered a type IV isotherm with two closed hysteresis loops typical for mesoporous structures (Figure 3a,b). At low relative pressure, monolayer adsorption takes place. This is followed by multilayer adsorption and a strong increase in the adsorption at $p/p_0 = 0.2$, indicating the filling of the mesopores by capillary condensation. The second noticeable

increase in the adsorbed volume occurs at relative pressures above 0.8. The hysteresis loop is caused by interparticular pores present due to the nanometer-sized particles and by pore blocking or cavitation effects.[19] The BET surface area determined in this way is 1000 $m^2 \cdot g^{-1}$, and the total pore volume was found to be 1.2 $mL \cdot g^{-1}$. The BJH analysis delivers a narrow nanopore size distribution with a maximum at 3 nm and no further peaks at higher values which would correspond to larger pores.

Inhibitor Loading and Release. For the loading step, a dispersion of MS-SiO_2-NPs in water saturated with the corrosion inhibitor 1*H*-benzotriazole (BTA) was prepared and stirred for 2 h under reduced pressure. This latter technique has previously been found to be beneficial in increasing loading.[20−24] The loading efficiency can be estimated using N_2 sorption by observing the change in nanoparticles' porosity and reduction in total pore volume. A decrease of the number of micropores leading to higher average pore diameter was detected after loading. Thus, the decrease of the total pore volume can be assigned to the loaded BTA molecules in the mesopores of the silica network. Thus, a loading of 409 mg(BTA)/1 g(SiO_2) was found.

In order to assess whether this value is feasible, a theoretical maximum loading capacity for the loaded sample, given a total pore volume 1.122 $mL \cdot g^{-1}$, was calculated. Assuming that only the pores are filled with the benzotriazole molecules with a molar volume 87.6 $mL \cdot mol^{-1}$, the maximum theoretical loading capacity

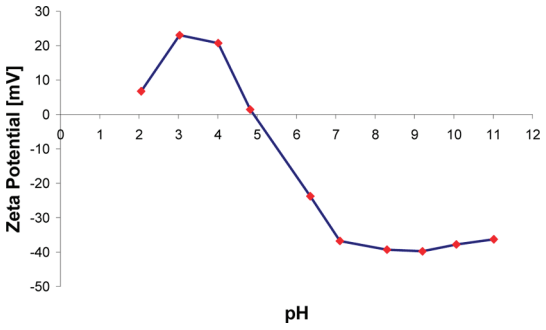

Figure 2. Zeta-potential dependence on pH of mesoporous silica nanoparticles.

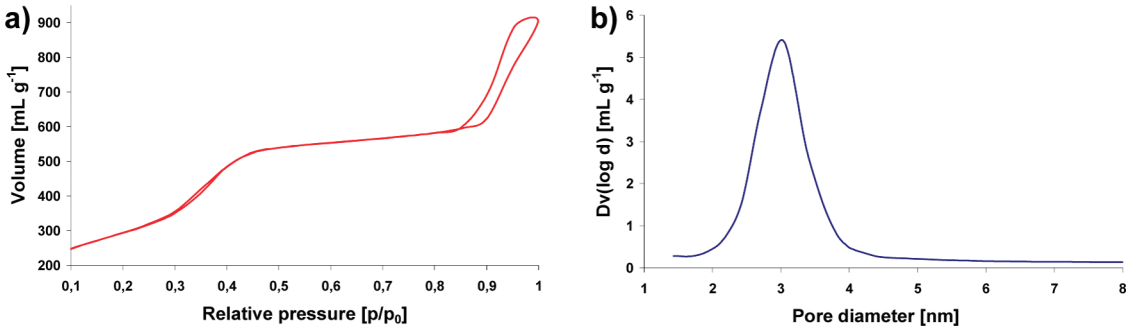

Figure 3. (a) N_2 sorption isotherm and (b) pore size distribution of mesoporous silica NPs.

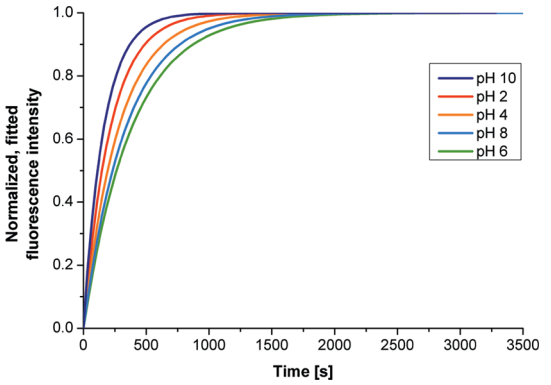

Figure 4. BTA release kinetics measured at different pH values.

is 1.53 g(BTA)/1 g(SiO_2). The achieved experimental loading is around one-third of the maximum one and is therefore reasonable but could be further optimized. It should be noted that the mesoporous silica nanocontainers presented in this work possess elevated uptake and encapsulating properties (two times higher loading) in contrast to the ones already reported in the literature for comparable nanocontainers.

The release kinetics of the above-described system with loaded inhibitor, amounting to 409 mg(BTA)/1 g(SiO_2), was investigated by fluorimetrical analysis of water suspensions of inhibitor-loaded silica nanocontainers. The fluorescence intensity was observed every 1 s for a time period of 1 h to ensure a precise detection of the release rate and reaching of the saturation level. The particle size leads to light scattering and a noisy signal. Therefore, to obtain quantitatively reliable data, the curves were fitted and an exponential fit was optimal (Figure 4). The fastest release could be observed at pH 10, followed by pH 2. In the first case, the maximum released amount could be reached within 160 s. In comparison, the time needed to achieve the saturation level at pH 6 is 2.4 times longer. At pH values different from neutral, both the silica particles as well as the inhibitor molecules have the same charge (positive at pH < 6 and negative at pH > 6). This leads to larger electrostatic repulsion forces and faster release. These results are very favorable for the subsequent application of the loaded silica nanocontainers in

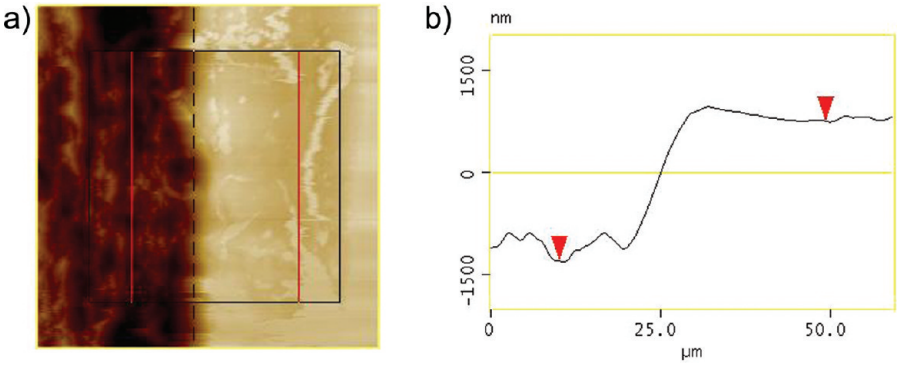

Figure 5. (a) AFM micrograph of an edge of AA2024 coated by a sol−gel film with loaded SiO_2-NPs, (b) average height section analysis.

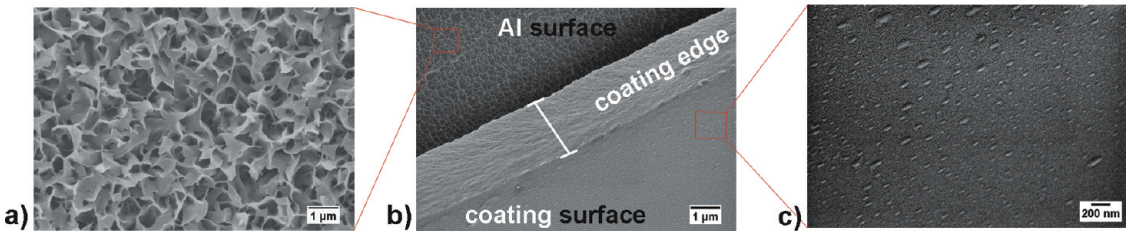

Figure 6. SEM micrographs of (a) ultrasonically pretreated aluminum substrate surface, (b) cross section of the aluminum substrate coated by SiO_x/ZrO_x layer with BTA-loaded silica nanocontainers, and (c) SiO_x/ZrO_x coating with BTA-loaded silica nanocontainers.

anticorrosive active coatings, as the corrosion is usually followed by alkaline or acidic pH shift. Thus, a release of the inhibitor in response to a pH change in the local environment is provided without the need for an additional polyelectrolyte shell as was employed before.

Characterization of the Coatings. The model metal substrate used in this work (aluminum alloy AA2024) was coated with a hybrid inorganic sol−gel (SiO_x/ZrO_x) employing the dip-coating technique. The atomic force microscopy (AFM) measurements of the sol−gel films (Figure 5a,b) indicate a thickness of approximately 2 μm for all possible compositions of the prepared sol−gel coatings. The SEM analysis (Figure 6) of the cross section of the Al alloy coated by sol−gel with loaded SiO_2-NPs shows a uniform coating thickness. The ultrasonic pretreatment of the substrate surface before coating increases its roughness and creates an active uniform aluminum oxide layer (Figure 6a). Furthermore, the incorporation and homogeneous distribution of the nanocontainers through the whole coating layer can be seen by SEM (Figure 6c). Due to the positioning of the sample during the SEM analysis, leading to stigmation effects, the incorporated silica NPs appear as ellipsoid islands (Figure 6c) with a size similar to those measured by TEM for the synthesized silica NPs alone. The uniform allocation of single and non-agglomerated silica nanocontainers in the SiO_x/ZrO_x coating was also revealed by AFM analysis of the film surface. In Figure 7, the nanocontainers are observed as evenly distributed higher peaks on the layer

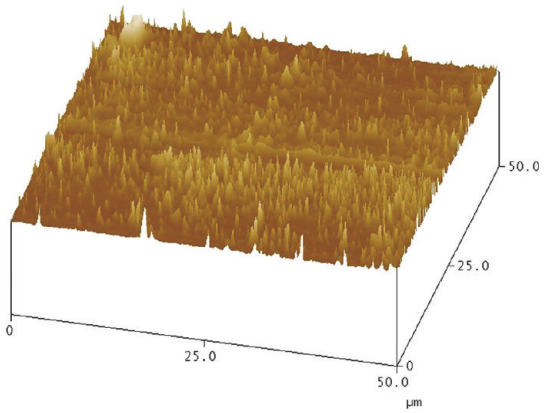

Figure 7. AFM topography of the surface of the SiO_x/ZrO_x coating containing silica nanocontainers loaded with BTA.

surface leading to average roughness of approximately 30 nm.

Anticorrosion Efficiency. To assess the protection efficiency of the anticorrosive active coatings with inhibitor-loaded silica nanocontainers, Al substrates without coating, coated with a SiO_x/ZrO_x film only, and coated with a SiO_x/ZrO_x layer incorporating (i) BTA and (ii) BTA-loaded silica NPs were immersed in 0.1 M NaCl solution for 10 days. Figure 8 shows the optical observation of corrosion in each of the above-described systems. The destructive corrosion effect can be clearly observed on the unprotected aluminum substrate (Figure 8a). The aluminum plate protected only by a SiO_x/ZrO_x coating (Figure 8b) shows low long-term corrosion resistance, and some defects as well as corrosion products can be

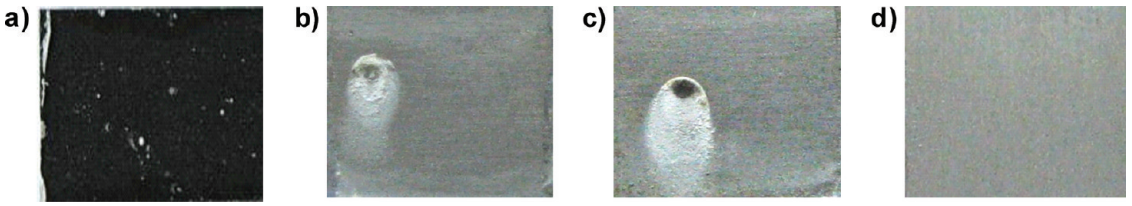

Figure 8. Optical photos of (a) pure aluminum substrate AA2024; (b) AA2024 coated with SiO_x/ZrO_x sol−gel and AA2024 protected by SiO_x/ZrO_x sol−gel film containing (c) BTA and (d) BTA-loaded SiO_2 nanoparticles.

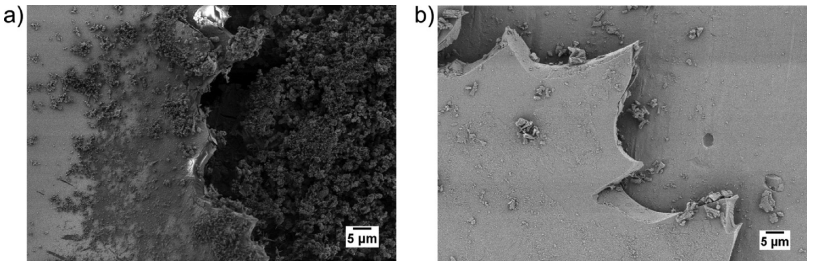

Figure 9. SEM micrographs of an aluminum substrate coated with (a) SiO_x/ZrO_x film and (b) SiO_x/ZrO_x film impregnated with BTA-loaded SiO_2 nanocontainers after 10 days of submersion in 0.1 M NaCl.

detected. The integrity of the sample coated with a SiO_x/ZrO_x layer and BTA was not preserved, either (Figure 8c). The directly integrated corrosion inhibitor performed insufficient passivation of the corrosive process possibly due to strong chemical bonding of the inhibitor molecules with the sol−gel coating matrix.[9] In contrast, the anticorrosive system consisting of a SiO_x/ZrO_x film containing BTA-loaded MS-SiO_2-NPs reveals no signs of corrosion even after 10 days of submersion in 0.1 M NaCl (Figure 8d). This clear difference from the other samples alongside the absence of any corrosion-induced defects confirms the high anticorrosion efficiency of such active, hybrid coatings incorporating inhibitor-loaded mesoporous silica nanocontainers. Their corrosion protective properties were investigated closer on a microscale by SEM. Figure 9 depicts the effect of the corrosive media (0.1 M NaCl solution) on the aluminum alloy when the protective coating system is manually scratched. When the AA2024 substrate is protected only by a SiO_x/ZrO_x sol−gel film, corrosion products are formed during the 10 day exposure to the solution. Figure 9a reveals that the parts with the manually introduced defects (*e.g.*, RHS of the image) in the coating are more aggressively attacked by the destructing corrosion process resulting in crystals of metal oxides or salts, covering the scratch. In comparison, the metal substrate protected by a SiO_x/ZrO_x coating containing BTA-loaded silica NPs reduces the corrosion rate and suppresses the destruction of the metal surface, which is indicated by the strong reduction in quantity of corrosion products. Figure 9b shows clearly that the metal surface is only minimally affected by the corrosive media, and its integrity and flat appearance are preserved.

To further study the self-healing and corrosion protection properties exhibited by the new hybrid coatings, current density measurements were carried out employing the scanning vibrating electrode technique (SVET). The corrosion process naturally causes a current flow, which is detected by the vibrating electrode moving above the metal surface. Therefore, the measured current density over an area can be plotted as a 3D current density map.[25−28] By indicating the minimum and maximum current density over the scanned area, a second plot can be drawn showing the change in current density with time. For this corrosion investigation, in order to induce and accelerate the corrosion process, a defect was introduced in the sol−gel coating. Scratches were made with a scalpel without spoiling the metal surface. The defect area typically has a length of 1 mm and a width of approximately 35 μm. The current density maps 15 min after immersion and after 10 h of exposure to the 0.1 M NaCl solution are presented for aluminum alloy coated with SiO_x/ZrO_x film, SiO_x/ZrO_x film with direct BTA inclusion, and SiO_x/ZrO_x film containing BTA-loaded SiO_2-NPs (Figure 10). The anodic activity measured after immersion of the coated substrates can be observed above the scratch and is assigned to the excess of Al^{3+} ions produced by the redox reaction between aluminum and oxygen from the water. A pitting corrosion site can be detected immediately after immersion in the case of the sample protected by a SiO_x/ZrO_x coating with direct BTA inclusion. An increase of the current density with time can be clearly observed for this sample as well as for the one coated only by a SiO_x/ZrO_x film (Figure 10a,b). In contrast, an obvious suppression of the development of the corrosion process in the samples coated with a sol−gel film containing inhibitor-loaded silica nanocontainers is found (Figure 10c). This good anticorrosive performance is shown by the absence of anodic activity and the low

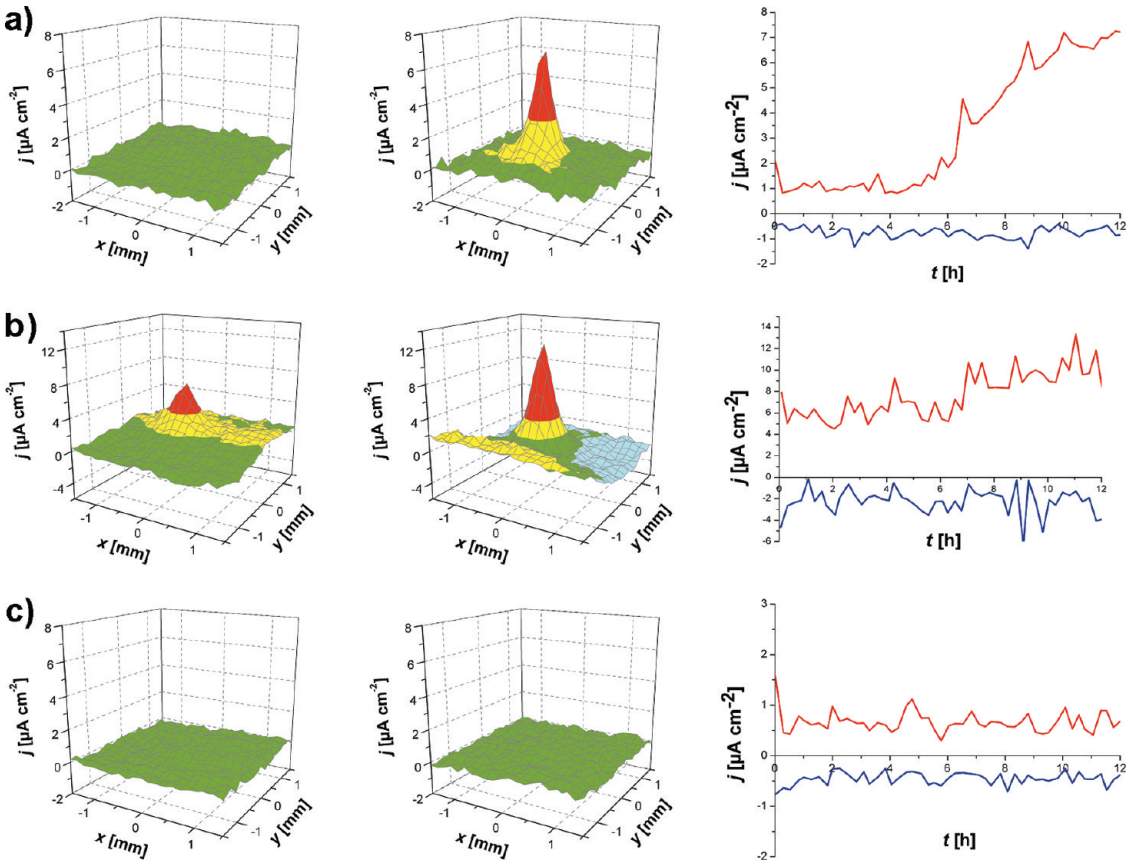

Figure 10. Left and middle: SVET current density maps of aluminum substrate coated with (a) SiO_x/ZrO_x film, (b) SiO_x/ZrO_x film with BTA, and (c) SiO_x/ZrO_x film containg BTA-loaded MS-SiO_2-NPs obtained after 15 min and 10 h. Right: Maximum and minimum current densities (*j*) *versus* time after immersion in 0.1 M NaCl over the scratched surface of the films with corresponding maps on the left and middle.

values of the anodic current. In the case of the sample with a coating containing inhibitor-loaded silica nanocapsules, the corrosion protection is triggered by the corrosion process itself. At increase or decrease of the local pH, the inhibitor is released from the mesoporous silica network in a sufficient amount, without undesired leakage, to stop the corrosion. The anticorrosive effect of the organic inhibitor 1*H*-benzotriazole is based on forming a dense film on the metal surface acting as a physical barrier for the aggressive medium. In addition, complexes with copper, which is one of the intermetallic inclusions of the Al alloy, are built and thus decreasing the anode−cathode pairs on the Al surface, followed by passivation of the anodic and cathodic activity.[10,11,29−32]

CONCLUSIONS

In this article, we have studied and evaluated the anticorrosion efficiency of a new, simplified active coating system consisting of a hybrid silica−zirconia film doped with 1*H*-benzotriazole-loaded mesoporous silica nanocontainers without an additional shell. The strategy consists of embedding porous nanoparticles in a coating. These nanoparticles are filled with corrosion inhibitors and released near a defect if it is formed, thus leading to self-repair. As a model, we studied an aluminum alloy and a coating frequently used and demonstrated that nanoparticles can be inserted with high inhibitor content and hence superior efficiency. We demonstrate the formation of porous silica NPs, providing the system superior anticorrosive efficiency, while maintaining a simple way of manufacturing. Since loading, release, and anticorrosion efficiency can be quantified, we can also contribute to an understanding of the mechanisms.

In more detail, the mesoporosity, monodispersity, and spherical morphology of the studied silica NPs favor their application as nanoreservoirs for corrosion inhibition. Thus, a loading efficiency much higher than the ones reported for similar systems was achieved. The incorporation of the loaded NPs in a SiO_x/ZrO_x sol−gel matrix was successful and resulted in homogeneous distribution of the nanocontainers and uniform coating thickness. The incorporated mechanically stable nanocarriers block the micropores, cracks, and areas with low cross-link density in the passive SiO_x/ZrO_x coating film and improve its physical barrier properties. Furthermore, due to the pH-stimulated release of inhibitor during the corrosion process, well-pronounced active anticorrosive properties and self-healing were provided and confirmed by SEM

and SVET measurements. The studied mesoporous silica NPs store the corrosion inhibitor and prevent it from undesired leakage and contact with the SiO_x/ZrO_x coating matrix. In addition, the complex porous system provides high loading capacity and quick inhibitor release on demand even without an additional shell.

The above presented and summarized results clearly provide evidence for the advantageous properties of the synthesized mesoporous silica nanocontainers and their function on improving the performance of active anticorrosive coatings.

EXPERIMENTAL SECTION

Materials. Tetraethyl orthosilicate (TEOS), hexadecyl trimethyl ammoniumchloride (CTACl 25% in H_2O), triethanolamine (TEA), (3-glycidyloxypropyl)trimethoxysilane (GPTMS), tetra-*n*-propoxyzirconium TPOZ (70 wt % in *n*-propanol), and 1*H*-benzotriazole (BTA) were purchased from Sigma-Aldrich (Germany). The solvents for the sol−gel (ethyl acetoacetate and propan-2-ol) were provided by Alfa Aesar and Merck, respectively. All chemicals were used as received. The milli-Q water used in all experiments was purified in a three-stage Millipore milli-Q Plus 185 purification system. The investigated metal substrate, aluminum alloy AA2024, was supplied by EADS Deutschland.

Synthesis. Mesoporous silica NPs were synthesized applying the procedure introduced by Möller *et al.*[17] A stock solution was prepared by mixing 64 mL of milli-Q water (3.55 mol), 10.5 mL of ethanol (0.179 mol), and 10.4 mL of a 25 wt % CTACl water solution (7.86 mmol). After stirring this mixture for 10 min at room temperature, 4.125 mL of TEA (0.031 mol; 1:1 TEOS/TEA ratio) was added and stirred until all TEA was dissolved, resulting in pH value around 11. Subsequently, 20 mL of this stock solution was heated to 353 K in an oil bath; 1.454 mL of TEOS (6.5 mmol) was added dropwise to the pretempered solution (within 1−2 min) under vigorous stirring. The mixture was refluxed at 353 K for 2 h. A white solution developed after 10 min. Finally, the mixture was cooled to room temperature. The pH had decreased to around 9. The molar ratio of the individual components of the reaction mixture was TEOS/CTACl/TEA/H_2O/EtOH = 1:0.27:1:137:6.2. The template extraction was conducted in ethanol/HCl mixture (15 mL HCl (37%)/150 mL ethanol) for 30 min in an ice bath under ultrasonic agitation (100 W, 35 kHz). The surfactant molecules were separated by centrifugation (49 000*g*, 20 min), and the solid cakes were repeatedly washed to obtain mesoporous silica NPs free of template.

Loading, Embedding, and Coating. The subsequent loading of the silica containers with a corrosion inhibitor was conducted under reduced pressure (50 mbar). The as-synthesized silica−water suspension (10 mg·mL^{-1}) was mixed with aqueous 1*H*-benzotriazole (BTA) solution (10 mg·mL^{-1}) in a volume ratio 1:1 and stirred for 2 h. The as-loaded containers were separated by centrifugation and dried overnight at 333 K.

The hybrid sol−gel matrix (SiO_x/ZrO_x) for the subsequent dip-coating of the aluminum alloy (AA2024) substrates was prepared as described by Zheludkevich *et al.*[6] The zirconium oxide sol was synthesized by hydrolyzing a 70 wt % tetra-*n*-propoxyzirconium (TPOZ) solution in *n*-propanol mixed with ethylacetoacetate (EAA) (volume ratio 1:1) at pH 0.5. The mixture was treated by sonication at room temperature for 20 min to cause complexation of the precursor. The second organosiloxane sol was prepared by hydrolyzing (3-glycidyloxypropyl)trimethoxysilane (GPTMS) in propan-2-ol by the addition of acidified water in a molar ratio (GPTMS/propan-2-ol/water) of 1:3:2. The formed zirconia-based sol was mixed under stirring with the organosiloxane sol in a 1:2 volume ratio. The final sol−gel mixture was stirred under ultrasonic agitation for 60 min and then aged overnight at room temperature. The sol−gel system was homogeneous and transparent with a light-yellow color.

Before coating, the metal substrates (1 × 2 cm) were pretreated in milli-Q water by sonication (20 kHz, 1000 W, 10 min). The so pretreated substrates were coated completely with sol−gel, sol−gel with BTA, and sol−gel with BTA-loaded silica containers. The last two suspensions with a concentration of 3 mg·mL^{-1} were produced by sonication for 1 min. The sol−gel films were produced by a dip-coating procedure by immersing the pretreated substrate in the respective sol−gel mixture for 100 s followed by controlled withdrawal at a speed of 2 mm·s^{-1}. After coating, the samples were cured at 130 °C for 1 h.

Characterization. The morphology, size, and pore structure of the synthesized particles were characterized by transmission electron microscopy (Zeiss EM 912 Omega). The sample in form of water suspension was pipetted on a coated copper grid, dried, and subsequently investigated with an accelerating voltage of 120 kV. Scanning electron microscopy (Zeiss Gemini LEO 1550) was employed to analyze silica samples as well as the coated Al alloy substrates. An operating voltage of 3 kV and different magnifications were applied. Dynamic light scattering (Malvern Zetasizer 4) was employed to measure the size and electrophoretic mobility of the samples. The obtained size data were further analyzed by the CONTIN model. The zeta-potential was measured using the Smoluchowski method and an auto mode. N_2 adsorption/desorption measurements at 77 K were performed on the system Micromeritics TriStar 3000 to study the porosity of the samples. These were pretreated by outgassing under vacuum at 423 K. When the BET and BJH model isotherms were applied, pore size distributions were obtained. The examination of the inhibitor release kinetics was carried out with the help of fluorescence spectroscopy (FluoroMax-4, HORIBA Jobin Yvon). Water suspensions of inhibitor-loaded silica NPs were prepared in an acryl cuvette directly before starting the measurement. The fluorescence intensity was observed every 1 s. Excitation was performed at 275 nm, and the emission was detected at 360 nm. The coating of the AA2024 plates was performed with Dip Coater RDC 15 (Bungard Elektronik). The immersion time was 100 s and the pull-up speed 2 mm·s^{-1}. Atomic force microscopy (Dimension 3100, Veeco Instruments) provided information about the surface topology and thickness of the SiO_x/ZrO_x films on Al alloy substrates.

For the characterization and quantification of the corrosion process in dip-coated aluminum alloy substrates, the scanning vibrating electrode technique (SVET, Applicable Electronics) was employed. This is based on the development of anodic and cathodic sites on the substrate surface induced by redox reactions during the corrosion process. Thus, an alternating current signal is induced due to the electrostatic potential gradient inside the electrolyte solution. A vibrating PtIr electrode with a vibrating Pt-blackened tip moves above the sample, scans its surface, and detects the current density. This is analyzed with a phase-sensitive detector and amplifier (PSDA). As a result, the peak-to-peak amplitude is recorded for different *x*−*y* positions of the tip above the sample to provide current density maps.

Prior to the measurement, the coated substrates are covered by adhesive tape (Tesa, clear, 60 μm thickness) to leave an uncovered exposure area of 3 × 3 mm^2. On this, a scratch (1 mm × 35 μm) was made with a scalpel without damaging the metal surface. The so pretreated metal plates were fixed on a glass holder and immersed into 0.1 M NaCl water solution. A Pt-blackened electrode tip with a diameter of 20 μm was moved at 300 μm above the substrate to detect the current intensity with time. The vibration frequency was set to 837 Hz, and the peak-to-peak amplitude was 150 μm. The analyzed sample area was scanned within *ca.* 5 min, and the scans were repeated every 15 min. The subsequent analysis of the SVET data was

performed with the help of homemade software to provide information about the minimal and maximal current densities in dependence of time.

Acknowledgment. We thank R. Pitschke for TEM images, R. Rothe for BET analysis, and D. Fix for SVET measurements. The authors acknowledge the financial support of the German Ministry of Education and Research (NanoFutur program), EU FP7 project "MUST" and Volkswagen Foundation.

REFERENCES AND NOTES

1. Liu, Z.; Chong, P. H.; Butt, A. N.; Skeldon, P.; Thompson, G. E. Corrosion Mechanism of Laser-Melted AA 2014 and AA 2024 Alloys. *Appl. Surf. Sci.* **2005,** *247*, 294–299.
2. Clark, W. J.; Ramsey, J. D.; McCreery, R. L.; Frankel, G. S. A Galvanic Corrosion Approach to Investigating Chromate Effects on Aluminum Alloy 2024-T3. *J. Electrochem. Soc.* **2002,** *149*, B179–B185.
3. Twite, R. L.; Bierwagen, G. P. Review of Alternatives to Chromate for Corrosion Protection of Aluminum Aerospace Alloys. *Prog. Org. Coat.* **1998,** *33*, 91–100.
4. Wang, H.; Akid, R. A Room Temperature Cured Sol−Gel Anticorrosion Pre-treatment for Al 2024-T3 Alloys. *Corros. Sci.* **2007,** *49*, 4491–4503.
5. van Ooij, W. J.; Zhu, D. Q.; Prasad, G.; Jayaseelan, S.; Fu, Y.; Teredesai, N. Silane Based Chromate Replacements for Corrosion Control, Paint Adhesion, and Rubber Bonding. *Surf. Eng.* **2000,** *16*, 386–396.
6. Zheludkevich, M. L.; Serra, R.; Montemor, M. F.; Salvado, I. M. M.; Ferreira, M. G. S. Corrosion Protective Properties of Nanostructured Sol−Gel Hybrid Coatings to AA2024-T3. *Surf. Coat. Technol.* **2006,** *200*, 3084–3094.
7. Palomino, L. M.; Suegama, P. H.; Aoki, I. V.; Montemor, M. F.; De Melo, H. G. Electrochemical Study of Modified Cerium-Silane Bi-Layer on Al Alloy 2024-T3. *Corros. Sci.* **2009,** *51*, 1238–1250.
8. Voevodin, N. N.; Balbyshev, V. N.; Khobaib, M.; Donley, M. S. Nanostructured Coatings Approach for Corrosion Protection. *Prog. Org. Coat.* **2003,** *47*, 416–423.
9. Raps, D.; Hack, T.; Wehr, J.; Zheludkevich, M. L.; Bastos, A. C.; Ferreira, M. G. S.; Nuyken, O. Electrochemical Study of Inhibitor-Containing Organic−Inorganic Hybrid Coatings on AA2024. *Corros. Sci.* **2009,** *51*, 1012–1021.
10. Palanivel, V.; Huang, Y.; van Ooij, W. J. Effects of Addition of Corrosion Inhibitors to Silane Films on the Performance of AA2024-T3 in a 0.5 M NaCl Solution. *Prog. Org. Coat.* **2005,** *53*, 153–168.
11. Zheludkevich, M. L.; Yasakau, K. A.; Poznyak, S. K.; Ferreira, M. G. S. Triazole and Thiazole Derivatives as Corrosion Inhibitors for AA2024 Aluminium Alloy. *Corros. Sci.* **2005,** *47*, 3368–3383.
12. Garcia-Heras, M.; Jimenez-Morales, A.; Casal, B.; Galvan, J. C.; Radzki, S.; Villegas, M. A. Preparation and Electrochemical Study of Cerium-Silica Sol−Gel Thin Films. *J. Alloys Compd.* **2004,** *380*, 219–224.
13. Zheludkevich, M. L.; Shchukin, D. G.; Yasakau, K. A.; Möhwald, H.; Ferreira, M. G. S. Anticorrosion Coatings with Self-Healing Effect Based on Nanocontainers Impregnated with Corrosion Inhibitor. *Chem. Mater.* **2007,** *19*, 402–411.
14. Shchukin, D. G.; Möhwald, H. Surface-Engineered Nanocontainers for Entrapment of Corrosion Inhibitors. *Adv. Funct. Mater.* **2007,** *17*, 1451–1458.
15. Skorb, E. V.; Fix, D.; Andreeva, D. V.; Möhwald, H.; Shchukin, D. G. Surface- Modified Mesoporous SiO_2 Containers for Corrosion Protection. *Adv. Funct. Mater.* **2009,** *19*, 2373–2379.
16. Fix, D.; Andreeva, D. V.; Lvov, Y. M.; Shchukin, D. G.; Möhwald, H. Application of Inhibitor-Loaded Halloysite Nanotubes in Active Anti-Corrosive Coatings. *Adv. Funct. Mater.* **2009,** *19*, 1720–1727.
17. Möller, K.; Kobler, J.; Bein, T. Colloidal Suspensions of Nanometer-Sized Mesoporous Silica. *Adv. Funct. Mater.* **2007,** *17*, 605–612.
18. Iler, R. K. *The Chemistry of Silica: Solubility, Polymerization, Colloid and Surface Properties, and Biochemistry*; John Wiley and Sons: New York, 1979; p 866.
19. Thommes, M.; Smarsly, B.; Groenewolt, M.; Ravikovitch, P. I.; Neimark, A. V. Adsorption Hysteresis of Nitrogen and Argon in Pore Networks and Characterization of Novel Micro- and Mesoporous Silicas. *Langmuir* **2005,** *22*, 756–764.
20. Lu, J.; Liong, M.; Zink, J. I.; Tamanoi, F. Mesoporous Silica Nanoparticles as a Delivery System for Hydrophobic Anticancer Drugs. *Small* **2007,** *3*, 1341–1346.
21. Hu, Y.; Cai, K.; Luo, Z.; Jandt, K. D. Layer-By-Layer Assembly of β-Estradiol Loaded Mesoporous Silica Nanoparticles on Titanium Substrates and Its Implication for Bone Homeostasis. *Adv. Mater.* **2010,** *22*, 4146–4150.
22. Cauda, V.; Schlossbauer, A.; Kecht, J.; Zürner, A.; Bein, T. Multiple Core−Shell Functionalized Colloidal Mesoporous Silica Nanoparticles. *J. Am. Chem. Soc.* **2009,** *131*, 11361–11370.
23. López-Noriega, A.; Arcos, D.; Vallet-Regí, M. Functionalizing Mesoporous Bioglasses for Long-Term Anti-Osteoporotic Drug Delivery. *Chem. Eur. J.* **2010,** *16*, 10879–10886.
24. Vallet-Regí, M.; Balas, F.; Arcos, D. Mesoporöse Materialien für den Wirkstofftransport. *Angew. Chem.* **2007,** *119*, 7692–7703.
25. Pratt, K. W., Jr; Johnson, D. C. Vibrating Wire Electrodes I. Literature Review, Design and Evaluation. *Electrochim. Acta* **1982,** *27*, 1013–1021.
26. Isaacs, H. S.; Davenport, A. J.; Shipley, A. The Electrochemical Response of Steel to the Presence of Dissolved Cerium. *J. Electrochem. Soc.* **1991,** *138*, 390–393.
27. Worsley, D. A.; McMurray, H. N.; Belghazi, A. Determination of Localised Corrosion Mechanisms Using a Scanning Vibrating Reference Electrode Technique. *Chem. Commun.* **1997,** 2369–2370.
28. He, J.; Gelling, V. J.; Tallman, D. E.; Bierwagen, G. P. A Scanning Vibrating Electrode Study of Chromated-Epoxy Primer on Steel and Aluminum. *J. Electrochem. Soc.* **2000,** *147*, 3661–3666.
29. Milic, S. M.; Antonijevic, M. M. Some Aspects of Copper Corrosion in Presence of Benzotriazole and Chloride Ions. *Corros. Sci.* **2009,** *51*, 28–34.
30. Kosec, T.; Merl, D. K.; Milosev, I. Impedance and XPS Study of Benzotriazole Films Formed on Copper, Copper-Zinc Alloys and Zinc in Chloride Solution. *Corros. Sci.* **2008,** *50*, 1987–1997.
31. Sutter, E. M. M.; Fiaud, C.; Lincot, D. Electrochemical and Photoelectrochemical Characterization of Naturally Grown Oxide Layers on Copper in Sodium Acetate Solutions with and without Benzotriazole. *Electrochim. Acta* **1993,** *38*, 1471–1479.
32. Qafsaoui, W.; Huet, F.; Takenouti, H. Analysis of the Inhibitive Effect of BTAH on Localized Corrosion of Al 2024 from Electrochemical Noise Measurements. *J. Electrochem. Soc.* **2009,** *156*, C67–C74.